IEEE Open Journal of the
Industrial Electronics Society

Received 10 November 2025; revised 12 December 2025; accepted 13 December 2025. Date of publication 16 December 2025;
date of current version 31 December 2025. The review of this article was arranged by Associate Editor Jorge Solsona.

Digital Object Identifier 10.1109/OJIES.2025.3644913

MPC-Based Multifunctional V2G Operation in Multienergy Systems

CHUAN LI[1,2] (Student Member, IEEE), **DANIELE CARTA**[1] (Member, IEEE), **EDOARDO DE DIN**[1] (Member, IEEE), AND **ANDREA BENIGNI**[1,2,3] (Senior Member, IEEE)

[1]ICE-1: Energy Systems Engineering, Forschungszentrum Jülich, 52428 Jülich, Germany
[2]RWTH Aachen University, 52056 Aachen, Germany
[3]JARA-Energy, 52425 Jülich, Germany

CORRESPONDING AUTHOR: CHUAN LI (e-mail: chu.li@fz-juelich.de).

This work was supported by the German Federal Ministry of Education and Research under Grant 03SF0628.

ABSTRACT This article presents an operational strategy for Vehicle-to-Grid (V2G) capable charging stations in multienergy systems (MESs). We present a novel model-predictive control (MPC) formulation based on the operation of four-quadrant charging stations and the behavior of electric vehicle drivers. The presented approach enables V2G capable charging units to serve multiple functions, including voltage regulation, power loss reduction, and MES energy management. Thus, the proposed MPC approach reduces violations of operational limits and improves the efficient use of MES components, such as photovoltaic systems and heat pumps. MPC with a V2G mode regulator is implemented to ensure efficient real-time operation of the MES. The proposed strategy is evaluated using a realistic MES inspired by the Forschungszentrum Jülich campus. Further tests conducted on a modified version of the IEEE 123-bus system demonstrate the scalability of the proposed V2G algorithm.

INDEX TERMS Distribution network, electric vehicles (EVs), model-predictive control (MPC), multienergy systems (MESs), vehicle-to-grid (V2G).

NOMENCLATURE

Sets and Indices

t, T_ω	Control interval of the MES operator, $t \in T_\omega$.
ϕ, Φ	Indices of thermal nodes, $\phi \in \Phi$.
θ	Index of MES thermal components.
H	Thermal power injected at the node.
i, j, f, n, N	Indices of electrical nodes, $i, \ldots, n \in N$.
ij	Index of electrical branches from node i to node j.
k, T_s	Discrete time step or control interval.
l	Index of load demand in the electrical and thermal networks.
m	Index of MES electrical components.
P/Q	Active/reactive power injected at the node.
p/q	Active/reactive power flow in the branch.

Parameters

$\alpha/\beta/\gamma$	Empirical power loss parameters of V2G chargers.
$\eta_{\text{ch/dch}}$	Charging/discharging efficiency of V2G chargers.
Γ_{1-4}	V2G contract parameters.
μ_e/σ_e	Mean/standard deviation of Gaussian distribution.
ρ_r	r-type of V2G contract.
$c_t^{e/\text{gas}}$	Day-ahead electricity/gas prices at time t.
c_t^{v2g}	V2G operation cost at time t.
DIS_r	Maximum discharge cycles of EV batteries in the r-type V2G contract.
$E_{j,\text{v2g}}$	Battery capacity of V2G EVs at node j.
k_c/k_p	Control/prediction horizon in MPC.
$P^{cs}_{j,\text{v2g}}/Q^{cs}_{j,\text{v2g}}$	Maximum active/reactive power of V2G chargers.
PLUG_r	Minimum daily plug-in time of EVs in the r-type V2G contract.
REM_r	Remuneration in the r-type V2G contract.
$\text{SoC}^{\text{min/max}}_{\text{v2g}}$	Minimum/maximum SoC of EV batteries during V2G operation.

$\mathrm{SoC}_r^{\min}$	Minimum SoC of EV batteries in the r-type V2G contract.
$t^{\mathrm{ari}}/t^{\mathrm{dep}}$	Arrival/departure time of EVs.
$z_{j,\mathrm{v2g}}^{P}/z_{j,\mathrm{v2g}}^{Q}$	Binary value indicating active/reactive power of V2G is activated.
$\mathrm{SoC}^{\mathrm{ini}}$	Initial SoC of EV batteries.
η	Transfer efficiency of MES components.
ψ_e	Gaussian distribution model of EVs.
$\tau^{P/Q}$	Time constant for the active/reactive power response of V2G converters.
$\tau_1^{\theta}/\tau_2^{\theta}$	First-/second-order time constant for the θth thermal component.
r_{ij}/x_{ij}	Resistance/reactance of branch ij.

Variables

P_j^{loss}	Total power loss variation in EDN caused by power injection at node j.
$\Delta P_{j,\mathrm{EDN}}^{\mathrm{loss}}$	Line loss variation in EDN caused by power injection at node j.
I_c/V_c	Current/voltage of V2G converters.
$P_{\mathrm{v2g}}^{\mathrm{ref}}/Q_{\mathrm{v2g}}^{\mathrm{ref}}$	Reference inputs for the active/reactive power of V2G chargers.
$P_{\mathrm{Conv}}^{\mathrm{loss}}$	Active power losses of V2G chargers.
$\mathrm{SoC}_j(k)$	Discrete state-of-charge of EV batteries.
$H_{\theta}^{\mathrm{ref}}$	Reference thermal power output of thermal components.
I_{ij}	Current through branch ij.
$P_{\mathrm{v2g}}^{\mathrm{ch/dch}}/Q_{\mathrm{v2g}}$	Active/reactive power of V2G.
v_j	Voltage at node J.

I. INTRODUCTION

The adoption of electric vehicles (EVs) has surged in recent years, driven by global governmental targets for transport decarbonization [1]. This increase necessitates the expansion of EV charging infrastructure in power distribution networks (DNs). Compared to conventional unidirectional EV charging stations (EVCSs), bidirectional power converters offer a more promising solution for managing the large power demands of EVs, as they can both consume and deliver power [2]. Thus, Vehicle-to-Grid (V2G) technology, which integrates EVs into grid operations, has been proposed and has become a hot topic.

The increasing penetration of EVs in power DNs poses various challenges to system operation [3]. To maintain grid stability, as mandated by distribution system operators, smart power management for EVs has become essential. In conventional and V2G EVCSs, the active power regulation is well established and utilized in power system operations, such as peak shaving [4], [5], active filtering [6], current balancing [7], and frequency regulation [8]. In addition, research in [9] revealed that V2G chargers can also provide reactive power compensation, aiding in power system stability improvement like voltage regulation. However, since the reactive power of V2G is limited by both the active charging demand and the total charger capacity, relying only on reactive power for voltage control is not sufficient [10]. Moreover, due to the low X/R ratio in DNs, active power compensation for voltage control can be as effective as reactive ones [11]. Therefore, the four-quadrant power property of V2G charging stations should be properly studied, as well as its potential benefits in cooperation with other energy components.

In recent years, multienergy systems (MESs) have shown advancements in integrating diverse energy forms to optimize overall system performance and sustainability, making them well suited for local energy communities [12]. Preliminary research indicates that V2G capable charging stations treated as energy storage systems can increase the efficient use of other energy units in the MES [13]. A similar study [14] has shown that integrating heat pumps (HPs) with battery and photovoltaic systems (PVs) can prevent network overloading. In [15], the V2G and human factors are considered in EVCS placement. This article notes that V2G activities not only complement electrical resources in MES but also improve the utilization of thermal units such as HPs. However, the simultaneous control of V2G and its integration with other energy units in MES still lacks further research.

In V2G operation, real-time control refers to the controller's ability to compute and implement optimal V2G decisions within limited time constraints. In the present work, the control actions are assumed to operate on a time scale ranging from seconds to minutes, depending on the problem size. As a result, the optimization of V2G in the MES under short time horizons significantly increases the computational complexity [16]. The optimal use of V2G depends not only on the network's topology, constraints, and MES objectives, but also on EV limits, such as battery degradation, state-of-charge (SoC), and EV drivers' interactions [15]. In this context, model-predictive control (MPC), characterized by its receding horizon and revising feedback, proves to be effective in managing these complexities [17], [18], [19]. Lu et al. [17] present an MPC-based algorithm that coordinates V2G scheduling to optimize power flow while considering both range anxiety and battery degradation. In [18], an MPC is developed to control V2G inverters by identifying parameters to mitigate the frequency deviations in microgrids. Similarly, Ke et al. [19] employ an MPC-VSG approach for EV stations to regulate microgrid frequency based on synchronous generators. However, none of these studies assess the real-time performance of their MPC for practical V2G deployments, and their V2G modeling remains limited to EV batteries, without considering its interaction with the MES.

Compared to centralized frameworks, distributed model-predictive control (DMPC) with lower computational burdens and real-time capabilities has been explored in V2G control [20], [21]. Research in [20] presents a noncooperative DMPC to manage EV chargers for energy scheduling in realistic energy communities. This approach leverages Nash equilibrium and game theory to find the agreement between EVs and prosumers. Similarly, a DMPC to regulate the reactive power of V2G for real-time voltage control is established in [21]. However, these systems rely heavily on advanced communication technologies and assume that each controller has access to the entire system's information. This implies that as V2G scales, the communication latency could become substantial and the global optimum may not be guaranteed [20]. In addition, the Jacobian matrix used for power flow calculations in aforementioned DMPCs must be rebuilt and inverted at every sampling interval, which poses significant computational challenges for real-time control [21].

Based on the aforementioned analysis, the development of an MPC-based V2G framework must address both computational complexity and real-time performance. Hence, this article presents a multifunctional V2G operation strategy within the MES with real-time capabilities. The main contributions of this article are summarized as follows.

1) A multiobjective MPC algorithm is developed to optimize V2G operations. The four-quadrant power of the V2G chargers is implemented considering EV constraints, such as battery degradation, V2G agreements, and driver interactions. Compared with existing approaches, the proposed MPC introduces a real-time mode regulator and linearized network modeling, enabling multifunctional control (voltage regulation, power loss reduction, and MES cost optimization) with low computational complexity, which enables real-time implementation in large-scale systems.
2) The proposed V2G serves as a dynamic energy storage system, coordinated with an aggregator named "V2G operator." The aggregator coordinates V2G-enabled EVs into a unified resource, thereby addressing system constraints and mitigating driving-related uncertainties such as range anxiety. Moreover, the V2G cooperates with the MES to improve the efficient use of multienergy resources, such as PVs and HPs.
3) The proposed V2G framework is tested using real load and generation profiles obtained from the campus, along with realistic EV profiles.

The rest of this article is organized as follows. Section II describes the methodology. Section III introduces the system model. Section IV details the MPC formulation. Section V presents the case studies. Finally, Section VI concludes this article.

II. METHODOLOGY

This article studies an MES featuring both conventional and V2G EVCSs, as shown in Fig. 1. The system integrates PVs, wind turbines (W), battery storage (BAT), boilers (B), thermal storage (TS), and external grid connections. The energy exchange between thermal and electrical networks is done by HPs and combined heat and power (CHP). The gas and heat pipelines are shown in green and red, respectively, and the black lines represent the electric cables. The dashed blue line indicates V2G information, such as measurement and control signals.

A hierarchical approach is used to operate the MES. All components, excluding V2G, are managed by a system operator responsible for ensuring optimal economic operation while adhering to MES constraints. V2G serves as an extra resource primarily to mitigate MES operating issues (e.g., voltage violation and power mismatch) and secondarily to further improve economic efficiency.

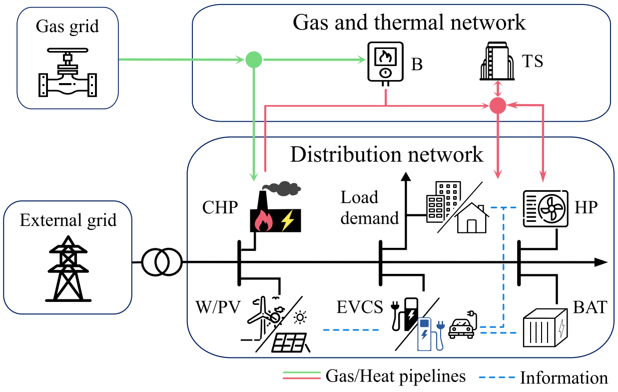

FIGURE 1. **V2G operation in the MES.**

The objective of this study is to develop a V2G operation strategy with multiple functions in the MES, while considering both technical and operational constraints. To achieve this, three key factors are considered.

First, the effective management of active and reactive power in V2G EVCSs mainly depends on the interactions with EVs [10]. Therefore, it is essential to model both the dynamic features of EV batteries (e.g., SoC) and the uncertainties in EV driver behavior, such as arrival time, departure time, and initial battery state. Moreover, the V2G agreement problem between EV drivers and operators must be considered.

Second, the implementation of V2G enhances MES performance in several aspects, such as improving voltage profiles, reducing operational costs, and allowing other energy components (e.g., PV, CHP, and HPs) to operate with greater flexibility [21], [22]. Thus, a multiobjective function for determining the appropriate V2G activities should be discussed.

Third, solving MPC problems on a real-time horizon is challenging when full-scale V2G converters, EV driving profiles, and MES constraints are included [15]. To alleviate the computational burden, model linearization algorithms are applied, such as system-level modeling of V2G converters and linearized power flow models of distribution networks.

Consequently, a multifunctional MPC is designed to manage V2G operations in the MES, as shown in Fig. 2. The top part outlines the operation of MES, and the bottom dashed area shows the proposed V2G strategy. The process begins with V2G providing available power data (P/Q_{V2G}) to the MES operator, allowing the MES to optimize its generation (P/Q_{MES}) by benefiting from V2G inputs. Subsequently, the optimized MES outputs are shared back to the V2G operator, enabling V2G to refine its control objectives. In this way, MES optimization takes priority and guides V2G operations, while initial V2G data provide support for the MES.

At the top, the MES operator first collects day-ahead forecasts (e.g., weather conditions, electricity and gas prices, and

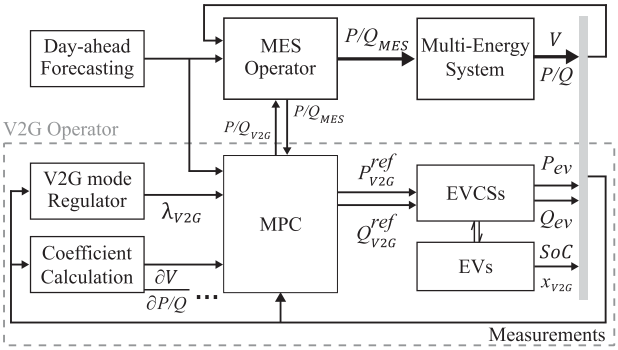

FIGURE 2. Block diagram of the proposed framework.

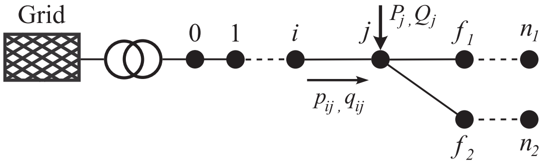

FIGURE 3. Diagram of the radial distribution network.

system constraints) and closed-loop measurements. Next, it receives data on the available power from V2G (P/Q_{V2G}). Using these inputs, the operator optimizes the MES generation (P/Q_{MES}). Then, this optimized value is exchanged with the V2G operator (MPC) to enhance V2G operation and avoid overlapping control.

The bottom part illustrates the functions of the V2G operator. At the beginning of each control interval, the EV statues, such as the SoC and P/Q_{ev}, are measured by the EVCSs and sent to the MPC controller. The V2G mode regulator then selects the appropriate V2G control objectives, including voltage regulation, power loss reduction, and energy management, based on the MES measurements. Simultaneously, the coefficient calculation block defines key V2G control parameters, such as voltage coefficients, power loss coefficients, and parameters for V2G-MES interaction, like surplus power storage and cost optimization.

Once these parameters are calculated, they are set as inputs to assist the MPC controller in determining the reference active and reactive power of V2G ($P^{\text{ref}}_{\text{V2G}}/Q^{\text{ref}}_{\text{V2G}}$). Finally, these control signals are sent to the EV converters and the MES (right blocks) for optimal operation and real-time measurement.

III. MES MODELING

A. ELECTRICAL DISTRIBUTION NETWORK

In this article, the radial layout of the electrical distribution network (EDN) is employed [23], as shown in Fig. 3, where $N = \{0, 1, \ldots, n\}$ is the set of nodes, the variable $l_{ij} \in \mathcal{L}$, where $L = \dim(\mathcal{L})$ denotes the set of lines connecting nodes $i, j \in N$, and the symbol $f_{1,2,\ldots}$ represents all child buses from node j. Node 0 shows the slack bus of the network connected to the external power grid.

In power flow analysis, linearized models, such as the linearized branch flow model, are widely applied to reduce the level of computation and to obtain a state-update model formulation that can be applied in the MPC structure [24]. Thus, this approach enables efficient optimization compatible with iterative MPC schemes for applications, such as voltage regulation and distributed energy resource integration. Moreover, it is reasonable to assume that line losses are small compared to the power flow in lines. Hence, a linearized branch flow model based on per-unit system is utilized to reduce the strong coupling and nonlinearity between voltage and power [25]

$$\sum_{f:j\rightarrow f} p_{jf} = p_{ij} - r_{ij}(p_{ij}^2 + q_{ij}^2) + P_j \tag{1a}$$

$$\sum_{f:j\rightarrow f} q_{jf} = q_{ij} - x_{ij}(p_{ij}^2 + q_{ij}^2) + Q_j \tag{1b}$$

$$v_i{}^2 - v_j{}^2 = 2(r_{ij}p_{ij} + x_{ij}q_{ij}) - (r_{ij}^2 + x_{ij}^2)I_{ij}{}^2 \tag{1c}$$

$$I_{ij}{}^2 = p_{ij}^2 + q_{ij}^2 \tag{1d}$$

where $v_i \in \mathbb{R}$ represents the voltage at node i, and $I_{ij} \in \mathbb{R}$ denotes the current in line l_{ij}. The variables $p_{ij}, q_{ij} \in \mathbb{R}$ indicate the active and reactive power flows from node i to node j. $r_{ij}, x_{ij} \in \mathbb{R}$ are the resistance and reactance of lines, respectively. The capital letters P_j/Q_j refer to active/reactive power injected at node j

$$P_j = \sum_m P_{m,j} + P_{l,j} \quad \text{and} \quad Q_j = \sum_m Q_{m,j} + Q_{l,j}$$

$$\forall m \in \{\text{CHP, W, PV, HP, BAT, V2G}\} \tag{2}$$

where $P_{m,j}, Q_{m,j} \in \mathbb{R}$ represent the active and reactive power generated by mth component at node j, separately, including CHP, W, PV, HP, BAT, and V2G. $P_{l,j}, Q_{l,j} \in \mathbb{R}$ means the electrical load demands at node j.

Based on the recurrence relations, (1) and (2) can be reformulated to express the relationship between the squared voltage and the power injections at each node

$$v_j{}^2 = G_j(\mathcal{P}, \mathcal{Q}, v_0^2) \quad \forall j \in N, j \neq 0 \tag{3}$$

where $\mathcal{P} = \left[P_1, P_2, \ldots, P_n\right]^T$ and $\mathcal{Q} = \left[Q_1, Q_2, \ldots, Q_n\right]^T$ indicate vectors of active and reactive power injections at each node, respectively, whereas v_0 is the voltage of the slack bus.

B. THERMAL DISTRIBUTION NETWORK

As shown in Fig. 1, a thermal network with $\Phi = \{1, \ldots, \phi\}$ nodes is modeled. This network includes thermal sources, such as CHP, HP, and B, as well as thermal demands. Thermal energy is delivered between nodes via water pipelines. To model the thermal energy flow, nodal balance equations are utilized [26]

$$\sum_\theta H_\theta \cdot \eta_\theta = \sum_{l\in\Phi} H_l \quad \forall\theta \in \{\text{CHP, HP, B}\} \tag{4}$$

where $H_l \in \mathbb{R}$ denotes the thermal demand. $H_\theta \in \mathbb{R}$ and $\eta_\theta \in \mathbb{R}$ represent the thermal generation and transfer efficiencies, separately, of each component, including CHP, HP, and B.

To capture the heat flow in thermal pipelines, a second-order transfer function in the Laplace domain, based on the Ho method [27], is applied. This model provides a practical way to analyze thermal dynamics in pipelines by assuming uniform fluid properties and constant flow rates while neglecting heat losses and pressure variations

$$H_\theta = \frac{H_\theta^{\mathrm{ref}}}{\left(\tau_1^\theta s + 1\right)\left(\tau_2^\theta s + 1\right)} \quad \forall \theta \in \{\mathrm{CHP}, \mathrm{HP}, \mathrm{B}\} \tag{5}$$

where $\tau_1^\theta \in \mathbb{R}$ and $\tau_2^\theta \in \mathbb{R}$ represent the first- and second-order time constants for the θth component, respectively. $H_\theta^{\mathrm{ref}} \in \mathbb{R}$ denotes the reference thermal generation of each unit.

For simplicity, the external gas grid is modeled as a direct connection supplying natural gas to the CHP and B.

C. EV DRIVER AND THE V2G CHARGING STATION

The modeling of EV drivers is divided into two parts: the random behaviors of EVs and the V2G contract between EV drivers and operators. First, the uncertainties of EVs mainly depend on EV driver behaviors, including the arrival time t^{ari}, departure time t^{dep}, and initial SoC of EV batteries $\mathrm{SoC}^{\mathrm{ini}}$. According to [15], these dynamics can be modeled using Gaussian distributions $\mathcal{N}$

$$\psi_e = \mathcal{N}\left(\mu_e, \sigma_e^2\right) \ \forall e \in \{t^{\mathrm{ari}}, t^{\mathrm{dep}}, \mathrm{SoC}^{\mathrm{ini}}\} \tag{6}$$

where μ_e and σ_e represent the mean and standard deviation, respectively, based on different driving patterns, such as commuter mode and city mode [15].

Second, based on [15], the so-called "V2G contract" is applied to model the V2G participation rate ρ_r among EV drivers. This participation rate is influenced by four key attributes: remuneration to EV owners (REM_r), maximum allowed daily discharge cycle (DIS_r), guaranteed daily minimum SoC ($\mathrm{SoC}_r^{\mathrm{min}}$), and agreed daily plug-in time (PLUG_r)

$$\rho_r = \Gamma_1 \mathrm{REM}_r + \Gamma_2 \mathrm{DIS}_r + \Gamma_3 \mathrm{SoC}_r^{\mathrm{min}} + \Gamma_4 \mathrm{PLUG}_r \tag{7}$$

where Γ_{1-4} denotes the V2G contract parameters, and the subscript r indicates the different level of each attributes. For example, with $r = [1, 2, 3, 4]$, $\mathrm{SoC}_r^{\mathrm{min}}$ indicates 100, 80, 50, 20% , PLUG_r represents the required daily connection times of 0, 4, 6, 8 h, and so on. These parameters are combined within the V2G contract using a multinomial logit model to determine ρ_r [15], reflecting how different contract terms (e.g., higher remuneration or longer plug-in time) influence the willingness of EV owners to participate in V2G activities. Once the V2G contract is settled, both the V2G EVs and system operators will operate according to these constraints. Moreover, the V2G participation rate ρ_r is not used in the MPC formulation but is applied only in the case study to determine the allocation and placement of conventional and V2G EVCSs.

Since this article focuses on a system-level perspective rather than detailed converter control, the dynamics of V2G chargers are simplified to a first-order transfer function in the Laplace domain. Considering the inherent time delay and dynamic response of converters, the four-quadrant power dynamics of V2G charger is modeled as follows [28]:

$$P_{\mathrm{v2g}}^{\mathrm{ch/dch}} = \frac{1}{1 + \tau^P \cdot s} P_{\mathrm{v2g}}^{\mathrm{ref}} \tag{8}$$

$$Q_{\mathrm{v2g}} = \frac{1}{1 + \tau^Q \cdot s} Q_{\mathrm{v2g}}^{\mathrm{ref}} \tag{9}$$

where $P_{\mathrm{v2g}}^{\mathrm{ch/dch}}$ represents the active power for charging or discharging EV batteries, while Q_{v2g} denotes the reactive power from V2G chargers. $P_{\mathrm{v2g}}^{\mathrm{ref}}$ and $Q_{\mathrm{v2g}}^{\mathrm{ref}}$ indicate the reference inputs for active and reactive power, respectively. $\tau^{P/Q}$ is the primary time constant defined by the feature of V2G converters [29]. In this article, it is assumed that each V2G charger is equipped with a single converter and can only connect to one EV at a time.

D. MES ENERGY MANAGEMENT SYSTEM

In MES operation, each component's generation is optimized at every MES control interval T_ω based on its operational cost, day-ahead forecasts, and measurements. Thus, the objective function for economic MES generation is defined as

$$\min \sum_{t \in T_\omega} \left(\sum_m P_{m,t} c_t^e + \sum_\theta H_{\theta,t} c_t^{\mathrm{gas}} + P_{\mathrm{v2g},t}^{\mathrm{ch/dch}} c_t^{\mathrm{v2g}} \right) \tag{10}$$

$$\forall m \in \{\mathrm{CHP}, \mathrm{W}, \mathrm{PV}, \mathrm{HP}, \mathrm{BAT}\} \quad \forall \theta \in \{\mathrm{CHP}, \mathrm{HP}, \mathrm{B}\}$$

where $P_{m,t}$ and $H_{\theta,t}$ denote the electric and thermal power generated by each component at time t, separately. c_t^e and c_t^{gas} represent the day-ahead electricity and gas prices, respectively. The V2G coefficient c_t^{v2g} is defined with a comparatively low value relative to the other coefficients. By doing so, the MES energy management system determines the cost-efficient generation of MES components while treating V2G as a priority resource that supports and enhances the overall MES performance.

Moreover, the operation of all components must comply with MES constraints, including power flow equations in (1) and (2), thermal load balance in (4), voltage and current limits in the next section, and MES capacity constraints, $P_{m,t} \in [P_m^{\mathrm{min}}, P_m^{\mathrm{max}}]$ and $H_{\theta,t} \in [H_\theta^{\mathrm{min}}, H_\theta^{\mathrm{max}}]$. In addition, to avoid the battery system (BAT) interfering with MES optimization, the SoC of BAT is fixed to the same value at the beginning and end of the day.

As this is not the main focus of this article, further details on the real-time operation of the MES can be found in [12] and [26].

IV. MPC FORMULATION

A. COEFFICIENT CALCULATION

Based on (3), the partial derivatives $\frac{\partial v_j^2}{\partial P_{j,\mathrm{v2g}}}$ and $\frac{\partial v_j^2}{\partial Q_{j,\mathrm{v2g}}}$, representing the coefficients of the squared voltage at node j with respect to active and reactive V2G power injections, can be calculated using the chain rule as

$$\frac{\partial {v_j}^2}{\partial P_{j,v2g}/Q_{j,v2g}} = \frac{\partial G_j(\mathcal{P}, \mathcal{Q}, v_0^2)}{\partial P_{j,v2g}/Q_{j,v2g}} \quad \forall j \in N \tag{11}$$

where $P_{j,v2g}$ and $Q_{j,v2g}$ indicate the active and reactive power of V2G injected at node j, respectively. Since this study focuses on V2G's impact on the MES, voltage coefficients with respect to slack bus variations, i.e., $\frac{\partial {v_j}^2}{\partial v_0^2}$, are neglected.

On the other side, the total power loss in the MES caused by V2G, including line losses and converter losses, is formulated as follows. First, the line losses in the EDN are defined as

$$P_{\text{EDN}}^{\text{loss}} = \sum_{ij \in \mathcal{L}} r_{ij} \left(p_{ij}^2 + q_{ij}^2 \right) / v_j^2 \tag{12}$$

where all symbols are identical in (1). This formulation is derived from the relationship between power flow and current in distribution lines, i.e., $I_{ij}^2 = (p_{ij}^2 + q_{ij}^2)/v_j^2$, and the line loss $P_{\text{EDN}}^{ij} = r_{ij} I_{ij}^2$. Therefore, this equation captures the total active power loss across all lines ($\sum_{ij \in \mathcal{L}}$) in the EDN. Using the fast sensitivity method [30], the line loss variation $\Delta P_{\text{EDN}}^{\text{loss}}$ due to active and reactive V2G power changes at node j can be expressed as

$$\begin{aligned} \Delta P_{j,\text{EDN}}^{\text{loss}} = {} & \Delta P_{j,\text{v2g}}^2 \sum_{j \in M_j^{\text{lpath}}} \frac{r_{ij}}{v_j^2} + 2 \Delta P_{j,\text{v2g}} \sum_{j \in M_j^{\text{lpath}}} \frac{r_{ij} p_{ij}}{v_j^2} \\ & + \Delta Q_{j,\text{v2g}}^2 \sum_{j \in M_j^{\text{lpath}}} \frac{r_{ij}}{v_j^2} + 2 \Delta Q_{j,\text{v2g}} \sum_{j \in M_j^{\text{lpath}}} \frac{r_{ij} q_{ij}}{v_j^2} \end{aligned} \tag{13}$$

where $M_j^{l\text{path}}$ denotes the number of lines on the path from node j to the slack bus.

Second, as V2G chargers are commonly modeled as controllable voltage source converters (VSCs) [31], the active power losses in V2G chargers can be represented as a quadratic polynomial function of the charging current I_c

$$P_{\text{Conv}}^{\text{loss}} = \left(\alpha + \beta \cdot I_c / I_r + \gamma \cdot (I_c / I_r)^2 \right) \cdot S_n \tag{14}$$

where $I_c = \frac{\sqrt{P_{v2g}^2 + Q_{v2g}^2}}{V_c}$ represents the charging current, and V_c is the converter voltage. I_r and S_n denote the rated current and apparent power, separately. α, β, and γ are empirical loss parameters [32].

According to (14), the converter loss is related to the V2G power injections P_{v2g}/Q_{v2g} and the converter voltage V_c. Thus, the converter loss coefficients $P_{\text{Conv}}^{\text{loss}}$ in terms of V2G power can be derived using the chain rule

$$\frac{\partial P_{\text{Conv}}^{\text{loss}}}{\partial P_{\text{v2g}}/Q_{\text{v2g}}} = \frac{\partial P_{\text{Conv}}^{\text{loss}}}{\partial I_c} \cdot \frac{\partial I_c}{\partial P_{\text{v2g}}/Q_{\text{v2g}}}. \tag{15}$$

Given that the converter voltage V_c typically runs around 1.0 p.u., the impact of voltage deviations, $\frac{\partial P_{\text{Conv}}^{\text{loss}}}{\partial V_c}$, can be neglected.

B. DISCRETE STATE-SPACE MODEL

MPC operates in discrete time steps to optimize system behavior. Thus, the continuous-time dynamics of the V2G chargers, given in (8) and (9), are discretized using the zero-order hold method with a sampling time T_s

$$P_{j,\text{v2g}}^{\text{ch/dch}}(k+1) = A^P P_{j,\text{v2g}}^{\text{ch/dch}}(k) + B^P P_{j,\text{v2g}}^{\text{ref}}(k) \tag{16}$$

$$Q_{j,\text{v2g}}(k+1) = A^Q Q_{j,\text{v2g}}(k) + B^Q Q_{j,\text{v2g}}^{\text{ref}}(k) \tag{17}$$

where $P_{j,\text{v2g}}^{\text{ch/dch}}(k)$ and $Q_{j,\text{v2g}}(k)$ indicate the active and reactive power outputs, respectively. $P_{j,\text{v2g}}^{\text{ref}}(k)$ and $Q_{j,\text{v2g}}^{\text{ref}}(k)$ represent the control input variables. The discrete-time state-space parameters are defined as follows:

$$\begin{aligned} A^P &= e^{-T_s/\tau^P}, \; B^P = \left(1 - e^{-T_s/\tau^P} \right) / \tau^P \\ A^Q &= e^{-T_s/\tau^Q}, \; B^Q = \left(1 - e^{-T_s/\tau^Q} \right) / \tau^Q. \end{aligned} \tag{18}$$

The discrete state-space equation for the SoC of EV batteries are modeled as

$$\begin{aligned} \text{SoC}_j(k+1) = \text{SoC}_j(k) + {} & \frac{P_{j,\text{v2g}}^{\text{ch}}(k) \eta_{\text{ch}} T_s}{E_{j,\text{v2g}}} \\ & - \frac{P_{j,v2g}^{\text{dch}}(k) T_s}{\eta_{\text{dch}} E_{j,\text{v2g}}} \end{aligned} \tag{19}$$

where $\eta_{\text{ch/dch}} \in \mathbb{R}$ is the charging/discharging efficiency, and $E_{j,\text{v2g}}$ is the battery capacity of V2G EVs.

In order to derive the iterative state-space model of the squared voltage magnitude used in the MPC, (1) is evaluated at two consecutive time steps. Since, as discussed in [33], the squared voltage magnitude at time k depends solely on the power injections at the same time step. Therefore, (1) is considered for V2G power injections at two following time steps, and the dynamics occurring between the two steady-state conditions are neglected. Based on (11), the squared voltage magnitude at node j, ${v_j}^2$, in response to active and reactive power injections from V2G chargers can be modeled as

$${v_j}^2(k+1) = \frac{\partial {v_j}^2}{\partial P_{j,\text{v2g}}} \Delta P_{j,\text{v2g}}^{\text{ch/dch}} + \frac{\partial {v_j}^2}{\partial Q_{j,\text{v2g}}} \Delta Q_{j,\text{v2g}} + {v_j}^2(k) \tag{20}$$

where $\Delta P_{j,\text{v2g}}^{\text{ch/dch}} = P_{j,\text{v2g}}^{\text{ch/dch}}(k+1) - P_{j,\text{v2g}}^{\text{ch/dch}}(k)$ denotes the change in active power between consecutive time steps. The reactive power change $\Delta Q_{j,\text{v2g}}$ is the same.

Similarly, the variation of power losses in (12)–(15) can be reformulated in discrete form

$$P_j^{\text{loss}}(k) = \Delta P_{j,\text{EDN}}^{\text{loss}} + \frac{\partial P_{\text{Conv}}^{\text{loss}}}{\partial P_{\text{v2g}}} \Delta P_{j,\text{v2g}}^{\text{ch/dch}} + \frac{\partial P_{\text{Conv}}^{\text{loss}}}{\partial Q_{\text{v2g}}} \Delta Q_{j,\text{v2g}}. \tag{21}$$

So far, the overall discrete-time state-space model, incorporating network voltages, power losses, V2G charger dynamics, and EV battery SoC, can be formulated as

$$\begin{aligned} \mathbf{x}(k+1) &= \mathbf{A}\mathbf{x}(k) + \mathbf{B}\mathbf{u}(k) \\ \mathbf{y}(k) &= \mathbf{C}\mathbf{x}(k) \end{aligned} \tag{22}$$

where

$$\mathbf{A} = \text{diag}\left(\mathbf{A}_{\mathbf{ch}}^P, \, \mathbf{A}_{\mathbf{dch}}^P, \, \mathbf{A}^Q, \, \mathbf{A}^{SoC} \right)$$

$$[6pt]\mathbf{B} = \begin{bmatrix} \mathbf{B}_{\mathbf{ch}}^P & \mathbf{0}_{\Pi \times \Pi} & \mathbf{0}_{\Pi \times \Pi} \\ \mathbf{0}_{\Pi \times \Pi} & \mathbf{B}_{\mathbf{dch}}^P & \mathbf{0}_{\Pi \times \Pi} \\ \mathbf{0}_{\Pi \times \Pi} & \mathbf{0}_{\Pi \times \Pi} & \mathbf{B}^Q \\ \mathbf{B}_{ch}^{SoC} & \mathbf{B}_{dch}^{SoC} & \mathbf{0}_{\Pi \times \Pi} \end{bmatrix}$$

$$
\begin{aligned}
&[6pt]\mathbf{C} = \begin{bmatrix} \frac{\partial {v_1}^2}{\partial P_{1,\mathrm{v2g}}} & \cdots & \frac{\partial {v_1}^2}{\partial P_{N,\mathrm{v2g}}} & \frac{\partial {v_1}^2}{\partial Q_{1,\mathrm{v2g}}} & \cdots & \frac{\partial {v_1}^2}{\partial Q_{N,\mathrm{v2g}}} \\ \frac{\partial {v_2}^2}{\partial P_{1,\mathrm{v2g}}} & \cdots & \frac{\partial {v_2}^2}{\partial P_{N,\mathrm{v2g}}} & \frac{\partial {v_2}^2}{\partial Q_{1,\mathrm{v2g}}} & \cdots & \frac{\partial {v_2}^2}{\partial Q_{N,\mathrm{v2g}}} \\ \vdots & \ddots & \vdots & \vdots & \ddots & \vdots \\ \frac{\partial {v_N}^2}{\partial P_{1,\mathrm{v2g}}} & \cdots & \frac{\partial {v_N}^2}{\partial P_{N,v2g}} & \frac{\partial {v_N}^2}{\partial Q_{1,\mathrm{v2g}}} & \cdots & \frac{\partial {v_N}^2}{\partial Q_{N,v2g}} \\ P^{\mathrm{loss}}_{1,P} & \cdots & P^{\mathrm{loss}}_{N,P} & P^{\mathrm{loss}}_{1,Q} & \cdots & P^{\mathrm{loss}}_{N,Q} \end{bmatrix} \\
&[6pt]\mathbf{x}(k) = \left[\mathbf{P_{ch}}(k)^T,\ \mathbf{P_{dch}}(k)^T,\ \mathbf{Q}(k)^T,\ \mathbf{SoC}(k)^T\right]^T \\
&[3pt]\mathbf{u}(k) = \left[\mathbf{P}^{\mathbf{ref.ch}}_{\mathrm{v2g}}(k)^T,\ \mathbf{P}^{\mathbf{ref.dch}}_{\mathrm{v2g}}(k)^T,\ \mathbf{Q}^{\mathbf{ref}}_{\mathrm{v2g}}(k)^T\right]^T \\
&[3pt]\mathbf{y}(k) = \left[v_1(k)^2,\ v_2(k)^2,\ \ldots,\ v_N(k)^2,\ P^{\mathrm{loss}}(k)\right]^T \\
&[3pt]\mathbf{P_{ch/dch}}(k) = \left[P^{\mathrm{ch/dch}}_{1,v2g}(k),\ \ldots,\ P^{\mathrm{ch/dch}}_{j,v2g}(k),\ \ldots,\ P^{\mathrm{ch/dch}}_{\Pi,v2g}(k)\right]^T \\
&[3pt]\mathbf{Q}(k) = \left[Q_{1,\mathrm{v2g}}(k),\ \ldots,\ Q_{j,\mathrm{v2g}}(k),\ \ldots,\ Q_{\Pi,\mathrm{v2g}}(k)\right]^T \\
&[3pt]\mathbf{SoC}(k) = \left[\mathrm{SoC}_1(k),\ \mathrm{SoC}_2(k),\ \ldots,\ \mathrm{SoC}_\Pi(k)\right]^T \\
&[3pt]\mathbf{P}^{\mathbf{ref.ch/dch}}_{\mathrm{v2g}}(k) = \left[P^{\mathrm{ref}}_{1,\mathrm{v2g}}(k),\ \ldots,\ P^{\mathrm{ref}}_{j,\mathrm{v2g}}(k),\ \ldots,\ P^{\mathrm{ref}}_{\Pi,\mathrm{v2g}}(k)\right]^T \\
&[3pt]\mathbf{Q}^{\mathbf{ref}}_{\mathrm{v2g}}(k) = \left[Q^{\mathrm{ref}}_{1,\mathrm{v2g}}(k),\ \ldots,\ Q^{\mathrm{ref}}_{j,\mathrm{v2g}}(k),\ \ldots,\ Q^{\mathrm{ref}}_{\Pi,\mathrm{v2g}}(k)\right]^T
\end{aligned}
\tag{23}
$$

with $\mathbf{A}^{P}_{\mathbf{ch/dch}} = \mathrm{diag}(A^P, \ldots, A^P) \in \mathbb{R}^{\Pi\times\Pi}$, $\mathbf{A}^{Q} = \mathrm{diag}(A^Q, \ldots, A^Q) \in \mathbb{R}^{\Pi\times\Pi}$, and $\mathbf{A}^{\mathrm{SoC}} = \mathrm{diag}(1, \ldots, 1) \in \mathbb{R}^{\Pi\times\Pi}$. The elements in B matrix are similar to those in A, except that $\mathbf{B}^{\mathrm{SoC}}_{\mathrm{ch/dch}} = \mathrm{diag}(\eta_{\mathrm{ch/dch}}, \ldots, \eta_{\mathrm{ch/dch}}) \in \mathbb{R}^{\Pi\times\Pi}$. The term $P^{\mathrm{loss}}(k)$ in $y(k)$ represents the total power losses caused by V2G EV operations, while $P^{\mathrm{loss}}_{1-N,P}$ and $Q^{\mathrm{loss}}_{1-N,P}$ in matrix $\mathbf{C}$ denote the power losses caused by active and reactive power injection, as defined in (21). $\mathbf{0}_{\Pi\times\Pi}$ indicates the $\Pi \times \Pi$ zero matrix. The symbol Π denotes the total number of V2G chargers.

C. MODEL CONSTRAINTS

For optimal operation of V2G chargers, various technical constraints are evaluated. First, to ensure that the MPC is feasible, the four-quadrant power outputs must align with the device capacities. Moreover, as V2G chargers produce active and reactive power only when the EV is connected [15], the EV connections and V2G agreements must be modeled

$$0 \le P^{\mathrm{ch/dch}}_{j,\mathrm{v2g}}(k) \le P^{cs}_{j,\mathrm{v2g}} z^{P}_{j,\mathrm{v2g}}(k) \tag{24}$$

$$-Q^{cs}_{j,\mathrm{v2g}} z^{Q}_{j,\mathrm{v2g}}(k) \le Q_{j,\mathrm{v2g}}(k) \le Q^{cs}_{j,\mathrm{v2g}} z^{Q}_{j,\mathrm{v2g}}(k) \tag{25}$$

$$z^{P}_{j,\mathrm{v2g}}(k) = \begin{cases} 1, & \text{if } t^{\mathrm{ari}}_j \le k \le t^{\mathrm{ari}}_j + \mathrm{PLUG}_{\mathrm{v2g}} \\ 0, & \text{else} \end{cases} \tag{26}$$

$$z^{Q}_{j,\mathrm{v2g}}(k) = \begin{cases} 1, & \text{if } t^{\mathrm{ari}}_j \le k \le t^{\mathrm{dep}}_j \\ 0, & \text{else} \end{cases} \quad \forall j \in N \tag{27}$$

where $P^{cs}_{j,\mathrm{v2g}}$ and $Q^{cs}_{j,\mathrm{v2g}}$ are the maximum power of V2G chargers. The binary variable $z^{P}_{j,\mathrm{v2g}}(k)$ indicates whether the EV at node j is connected to the EVCS and within the V2G active power operation period defined by the V2G contract, i.e., $[t^{\mathrm{ari}}_j, t^{\mathrm{ari}}_j + \mathrm{PLUG}_{\mathrm{v2g}}]$. In contrast, $z^{Q}_{j,\mathrm{v2g}}(k)$ denotes whether the V2G charger at node j is available for reactive power control, which remains active during the entire EV plug-in duration $[t^{\mathrm{ari}}_j, t^{\mathrm{dep}}_j]$.

In V2G chargers, the quadratic relationship between active and reactive power is defined as

$$P^{\mathrm{ch/dch}}_{j,\mathrm{v2g}}(k)^2 + Q_{j,\mathrm{v2g}}(k)^2 \le {S^{cs}_{j,\mathrm{v2g}}}^2 \tag{28}$$

where $S^{cs}_{j,\mathrm{v2g}}$ is the apparent power of V2G chargers.

Second, under the V2G contract defined in (7), the SoC constraints for EV batteries are as follows:

$$\mathrm{SoC}^{\mathrm{min}}_{\mathrm{v2g}} \le \mathrm{SoC}_{\mathrm{v2g}}(k+1) \le \mathrm{SoC}^{\mathrm{max}}_{\mathrm{v2g}}. \tag{29}$$

At each control interval, the V2G battery degradation cost is negligible compared to the MES operation cost. Since this cost is already compensated through the V2G contract remuneration (REM_r), battery degradation in V2G operation is modeled as a constraint determined by the number of discharge cycles (DIS_r) specified in (7)

$$\sum_{k\in\mathcal{K}} \left(P^{\mathrm{ch}}_{j,\mathrm{v2g}}(k) + P^{\mathrm{dch}}_{j,\mathrm{v2g}}(k)\right) T_s \le \mathrm{DIS}_r E_{j,\mathrm{v2g}} \tag{30}$$

where $\mathcal{K}$ denotes the duration of V2G sessions, e.g., 24 h. DIS_r denotes the discharge cycle as defined by the V2G contract in (7).

In network constraints, the voltage and current of the EDN are limited to a safe range during V2G operation

$$\begin{aligned} v^{\mathrm{min}}_j &\le v_j(k) \le v^{\mathrm{max}}_j && \forall j \in N \\ 0 &\le |I_{ij}(k)| \le I^{\mathrm{max}}_{ij} && \forall ij \in \mathcal{L}. \end{aligned} \tag{31}$$

When V2G chargers interact with the MES, the extra charging and discharging limits for V2G EVs are defined as

$$\sum_{j\in N} P^{\mathrm{ch}}_{j,\mathrm{v2g}}(k) \le \sum_{\mathrm{MES}} P_m(k) - \sum_{j\in N} P_{l,j}(k), \text{ if } \mathbf{c}^{\mathrm{MES}} > 1 \tag{32}$$

$$\sum_{j\in N} P^{\mathrm{dch}}_{j,\mathrm{v2g}}(k) \le \sum_{j\in N} P_{l,j}(k) - \sum_{\mathrm{MES}} P_m(k), \text{ if } \mathbf{c}^{\mathrm{MES}} \le 1 \tag{33}$$

$$\mathbf{c}^{\mathrm{MES}} = \sum_{\mathrm{MES}} P_m(k) \Big/ \sum_{j\in N} P_{l,j}(k) \tag{34}$$

where $\sum_{\mathrm{MES}} P_m(k)$ is the active power generation of the MES, including CHP, W, and PV. $\sum_{j\in N} P_{l,j}(k)$ denotes the total load demand. The term c^{MES} represents the ratio of MES generation (excluding V2G) to the total load demand. Equation (32) ensures that when MES generation exceeds load demand (i.e., $c^{\mathrm{MES}} > 1$), the available surplus power can be stored in V2G EVs, and the maximum charging power is limited to this surplus value. Conversely, in (33), if generation is insufficient, the V2G service, i.e., discharging EVs, must not exceed the power mismatch between the MES and the overall load.

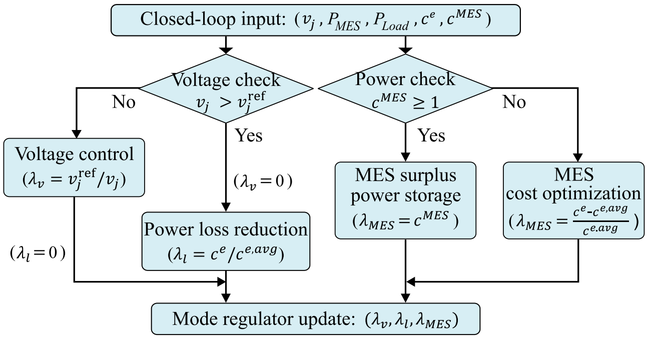

FIGURE 4. Flowchart of the V2G mode regulator.

D. OBJECTIVE FUNCTION

The multiobjective function for V2G operation over a prediction horizon k_p, balancing voltage regulation, power loss reduction, and MES cooperation, is defined as follows:

$$\min J = \sum_{k \in k_p} (\lambda_v \cdot O_v + \lambda_l \cdot O_l + \lambda_{\text{MES}} \cdot O_{\text{MES}}) \tag{35}$$

$$O_v = \sum_{j \in N} \left[v_j(k) - v_j^{\text{ref}} \right]^2 \quad O_l = \sum_{j \in N} P_j^{\text{loss}}(k)^2 \tag{36}$$

$$O_{\text{MES}} = \sum_{j \in N} P_{j,\text{v2g}}^{\text{dch}}(k) - P_{j,\text{v2g}}^{\text{ch}}(k) \tag{37}$$

where O_v, O_l, and O_{MES} represent the cost function for voltage regulation, power loss reduction, and MES cooperation, respectively. The weighting coefficients λ_v, λ_l, and λ_{MES} correspond to each cost function,with values assigned according to their relative importance. These coefficients are variable, and their specific values are determined based on the outcome of the V2G mode regulator presented in the next subsection. In (36), v_j^{ref} is the reference voltage of node j. The objective O_v indicates the specific voltage limit applied when voltage control is activated. The minus sign in (37) denotes the V2G benefits.

Moreover, the objective function $(\lambda_{\text{MES}} \cdot O_{\text{MES}})$ ensures that simultaneous charging and discharging are not possible at any time k. If a feasible solution to the optimization problem exists with both $P_{j,\text{v2g}}^{\text{dch}}(k) > 0$ and $P_{j,\text{v2g}}^{\text{ch}}(k) > 0$, there will always exist a lower cost solution that sets one to zero while adjusting the other accordingly [16].

E. V2G MODE REGULATOR

The weight factors λ_v, λ_l, and λ_{MES} are determined by a dynamic allocation algorithm, namely, the V2G mode regulator, as shown in Fig. 4. As can be seen, the prioritization of these objectives is divided into two aspects. In the left "voltage check," the first priority is to maintain the voltage of each node below the threshold v_j^{ref}. Once the "voltage control" becomes inactive, the V2G operates in the "power loss reduction" mode. Meanwhile, in the right-side "power check," since V2G cooperation with the MES can also affect the left part, it shares the same priority when either "voltage control" or "power loss reduction" is active. Initially, real-time MES data, including node voltage v_j, MES output P_{MES}, load demand P_{load}, and electricity prices (c^e, $c^{e,\text{avg}}$), are collected and fed into a series of decision blocks. Thus, the weighting of these objectives is calculated as follows.

1) Voltage check (left side):
   - *Case 1:* Voltage is below the reference ($v_j \leq v_{j,\text{ref}}$); prioritize "Voltage Control" with $\lambda_v = \frac{v_j^{\text{ref}}}{v_j}$, $\lambda_l = 0$. This case indicates that the MES generation is insufficient to meet the load demand, i.e., $c^{\text{MES}} \leq 1$. Therefore, "MES cost optimization" is activated ($\lambda_{\text{MES}} = \frac{c^e - c^{e,\text{avg}}}{c^{e,\text{avg}}}$) to determine how the active and reactive power of V2G can be utilized to regulate the voltage.
   - *Case 2:* Voltage is higher than reference ($v_j \geq v_{j,\text{ref}}$); activate "power loss reduction" based on electricity price c^e, $\lambda_l = \frac{c^e}{c^{e,\text{avg}}}$, $\lambda_v = 0$.
     This means that a higher electricity price (c^e) compared to the daily average price ($c^{e,\text{avg}}$) results in a higher power loss cost in (35).
     Meanwhile, based on (13), the cost of power loss O_l is relatively smaller compared to the V2G cost O_{MES}. Thus, the objective function in (35) mainly focuses on V2G power utilization, i.e., λ_{MES}. The weighting factor λ_l allows the controller to assess how V2G operation influences the electric distribution network.
2) Power check (right side):
   - *Case 1:* MES output exceeds load demand ($c^{\text{MES}} > 1$); store the surplus power in V2G EVs, $\lambda_{\text{MES}} = c^{\text{MES}}$.
   - *Case 2:* MES output is insufficient ($c^{\text{MES}} \leq 1$); perform "MES Cost Optimization" based on price differences, $\lambda_{\text{MES}} = \frac{c^e - c^{e,\text{avg}}}{c^{e,\text{avg}}}$.
     For example, if the current c^e is expensive ($c^e - c^{e,\text{avg}} > 0$), discharging V2G to meet load demand reduces costs compared to importing from the external grid. In contrast, when electricity is cheap ($c^e - c^{e,\text{avg}} < 0$), charging V2G EVs is cost effective, as they can store energy for later use during high-price periods.

In addition, the denominator $c^{e,\text{avg}}$ is used to maintain a similar range among λ_v, λ_l, and λ_{MES}.

F. OPTIMIZATION

The MPC solves a quadratic programming (QP) problem at each time step T_s. Based on (22), an augmented state-space model for V2G operation is rewritten as follows:

$$\begin{aligned} \mathbf{x_p}(k+1) &= \mathbf{A_p x_p}(k) + \mathbf{B_p} \Delta \mathbf{u_p}(k) \\ \mathbf{y}(k) &= \mathbf{C_p x_p}(k) \end{aligned} \tag{38}$$

where $\mathbf{x_p}(k+1) = [\mathbf{x}(k+1) - \mathbf{x}(k), \mathbf{y}(k)]^T$ and $\Delta \mathbf{u_p}(k) = \mathbf{u}(k) - \mathbf{u}(k-1)$ denote the increments of state variable and control input, accordingly. $A_p = [\begin{smallmatrix} A & 1 \\ CA & 1 \end{smallmatrix}]$, $B_p = [\begin{smallmatrix} B \\ CB \end{smallmatrix}]$, and $C_p = [0\ 1]$ indicate the augmented matrices. Thus, the cost

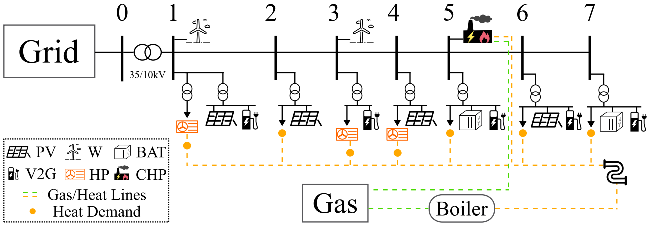

FIGURE 5. FZJ MES.

TABLE 1. Technical Parameters for MES Operation

MES unit	Capacity or maximum power	Efficiency	Operation cost [€/MWh]	Transfer time [s]
B	2 [MW]	0.92	c^{B}	$\tau_{1/2}$= 17/8
CHP	3 [MW]	0.76	c^{CHP}	$\tau_{1/2}$= 52/27
HP	1.2 [MW]	4[1]	c^{HP}	$\tau_{1/2}$= 9/4
PV	6 [MW]	0.90	c^{e}	-
W	2 [MW]	0.90	c^{e}	-
BAT	2.5 [MWh]	0.95	c^{e}	-
V2G	22 [kVA]	0.90	c^{e}	$\tau^{P/Q}$= 1

[1] The coefficient of performance (COP) of heat pumps.

function in (37) with prediction/control horizon k_p/k_c can be reformulated as

$$J = \sum_{\phi=1}^{k_p} x_p(k+\phi)^T \mathbf{Q} x_p(k+\phi) + \sum_{\phi=0}^{k_c-1} \Delta u(k+\phi)^T \mathbf{R} \Delta u(k+\phi) \tag{39}$$

where $\mathbf{Q} = \mathbf{C}_\phi{}^T \mathbf{C}_\phi$, and $\mathbf{C}_\phi = [\overbrace{0,\ldots,0}^{n_1}, 1]$ is the output matrix, with n_1 denoting the dimension of $\mathbf{x_p}(k)$. $\mathbf{R} = \mathrm{diag}(r_w, \ldots, r_w) \in \mathbb{R}^{k_c \times k_c}$, where $r_w \geq 0$ is the tuning parameter for the Δu performance. Hence, the optimal control input minimizing this objective function is obtained by setting $\frac{\partial J}{\partial \Delta u} = 0$. To solve the constraint problem in real time, Hildreth's quadratic algorithm is applied, as its ability to automatically recover from ill-conditioned cases is paramount for the safe operation of the plant [34]. In MPC, once closed-loop measurements are collected at each T_s, matrices $\mathbf{Q}/\mathbf{R}$ and state variables $x_p(k)$ are updated to reduce the prediction errors.

V. CASE STUDY AND DISCUSSION

In this study, an MES based on Forschungszentrum Jülich (FZJ) Living Lab Energy Campus is used to validate the proposed V2G algorithm, as shown in Fig. 5. The MES includes seven 10-kV nodes and 215 EV chargers. The load profiles are derived from existing measurements [35], and all loads are three-phase balanced. The day-ahead forecasts are taken from historical data [15]. Parameters for MES operation in (10), based on FZJ conditions, are listed in Table 1.

To evaluate the performance of the V2G, three test cases are introduced in Table 2. In Case 1, 215 conventional chargers are installed for immediate charging upon EV arrival, and the leaving SoC of all EVs is set to 100% . In Case 2, 122 conventional and 93 smart chargers are allocated. The smart chargers can only control the charging rate and charging time [35]. Compared to Case 2, 93 V2G chargers with multifunctionalities are installed in Case 3. Considering the study in [15], a practical V2G contract named "Moderate V2G" is applied in this article, with $\rho_{\mathrm{v2g}} = 38.5\%$, $\mathrm{DIS}_{\mathrm{v2g}} = 1$, $\mathrm{SoC}_{\mathrm{v2g}}^{\min} = 50\%$, and $\mathrm{PLUG}_{\mathrm{v2g}} = 6$ h. The evaluation of V2G contract and EVCS placement can also be found in the same study. Moreover, a VSC system employing Si-based IGBTs is used to model the power losses of V2G converters in (14), with parameters $\alpha = 0.0083$, $\beta = 0.003$, and $\gamma = 0.0032$ [32].

TABLE 2. Placement of Conventional/Smart/V2G EVCS in Each Case

Case	EVCS type	Node 1	Node 3	Node 5	Node 6	Node 7
1	uni	30/0	33/0	87/0	33/0	32/0
2	uni/smart	19/11	33/0	54/33	0/33	16/16
3	uni/V2G	19/11	33/0	54/33	0/33	16/16

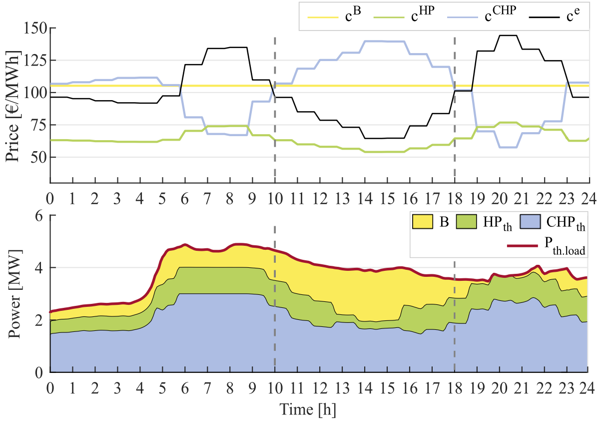

FIGURE 6. Case 1: 24-h operational cost (top) and thermal profile (bottom).

The EV driver behaviors are modeled based on historical patterns of FZJ employees, who typically arrive in the morning between 7:00 and 9:00, following a normal distribution. According to standard daily working hours, the leaving time of EVs is expected to fall between 16:00 and 18:00 [35]. Thus, the Gaussian distributions in (6) are defined as: $t^{\mathrm{ari}} = N(8, 0.4^2)$, $t^{\mathrm{dep}} = N(17, 0.4^2)$. For simplicity, all EVs are assumed to have the same lithium-ion batteries with 85 kWh [35]. Considering that the commuting distance between home and office varies between 10 and 80 km, with an EV consumption of 25 kWh/100 km and a 100% SoC at the start of the day from home, the initial SoC SoC^{ini} is assumed to range from 75% to 90% . In this article, all test cases are simulated on a real-time simulation platform based on OPAL-RT and Simulink, equipped with a 2.99-GHz processor and 64 GB of RAM, using a time step of 200 μs.

A. CASE 1: THE OPERATION OF THE MES WITHOUT V2G

Fig. 6 shows the 24-h operational cost of MES components and thermal profiles in Case 1. The top subplot presents

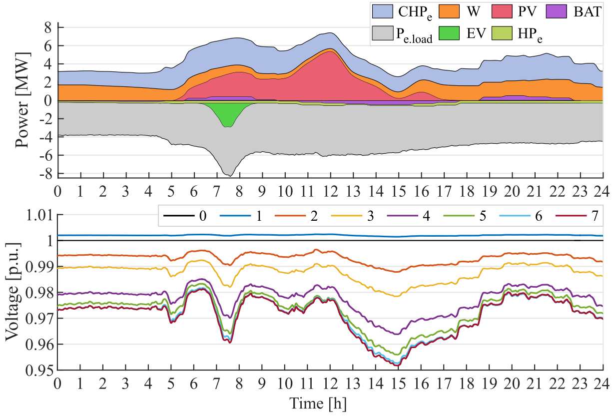

FIGURE 7. Case 1: 24-h electrical demand and supply profiles (top) and voltage curves (bottom).

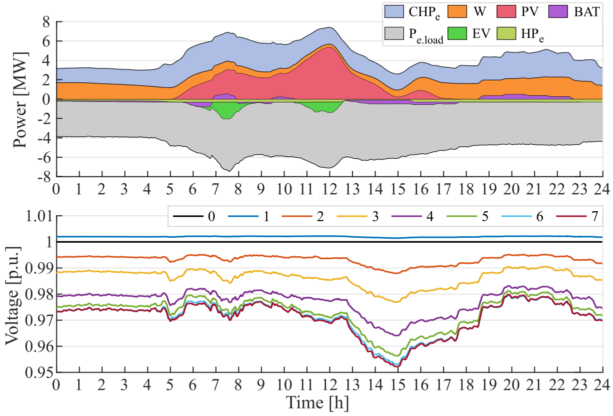

FIGURE 8. Case 2: 24-h electrical demand and supply profiles (top) and voltage curves (bottom).

the cost changes for B (yellow), HP (green), CHP (blue), and electricity (black). As can be seen, the electricity price and CHP cost fluctuate significantly, with peaks occurring at 6:00–10:00 and 11:00–18:00, separately. Other components, such as B and HP, remain relatively stable. These cost differences affect how different energy resources are utilized.

In the bottom subplot, thermal generations from B (yellow), HP_{th} (green), and CHP_{th} (blue) are plotted against the thermal demand (red line). At 6:00–10:00 and 18:00–23:00, the thermal demand is primarily met by CHP and HPs due to their low operational cost. However, between 13:00 and 16:00, HPs produce the least heat despite having the lowest cost. This occurs because node voltages, with $v^{\min} = 0.95$ p.u., cannot take extra load at this time (see Fig. 7), forcing the MES to generate more electricity from CHP to maintain safe operating conditions.

Fig. 7 shows the MES 24-h electrical load, supply, and voltage profiles. In the top subplot, positive values represent electricity generation, including CHP_{e} (blue), W (orange), PV (red), and BAT (purple). While negative values indicate consumption, such as load $\text{P}_{\text{e.load}}$ (grey), HP_{e} (pale green), and EV (green). The imbalance between MES supply and demand is compensated by the external grid. Due to the radial structure of the EDN (see Fig. 5), increased reliance on the external grid leads to high voltage drop in the network. For example, the bottom subplot shows a significant voltage drop at nodes 5, 6, and 7 during 7:00–9:00 and 13:00–18:00. The morning decline is mainly due to the extensive EV charging, while the afternoon drop is caused by insufficient MES generation.

B. CASE 2: OPERATION OF THE MES WITH SMART CHARGING

In this case, smart chargers are only used to optimize EV charging profiles and do not contribute to the cost-effective operation of MES thermal units, e.g., by discharging EVs to increase the network load capacity. Thus, the operation of the thermal network is identical to that in Fig. 6.

Fig. 8 shows the 24-h electrical load, supply, and voltage curves in Case 2. Compared to Case 1, the voltage drop at the morning period (7:00–8:00) is reduced. Based on the EV driving pattern in "commuter mode" with long-term connections, part of their charging demand can be shifted to around 12:00, absorbing the surplus power generated by the MES. However, since smart chargers cannot supply power, the voltage drop caused by insufficient MES generation from 13:00 to 17:00 still exists.

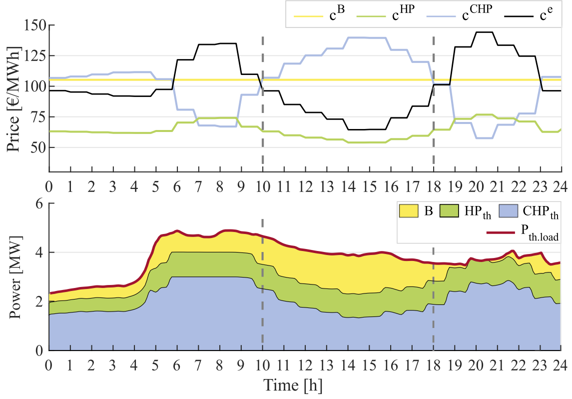

FIGURE 9. Case 3: 24-h operation cost (top) and thermal profile (bottom).

C. CASE 3: OPERATION OF THE MES WITH PROPOSED V2G

In Case 3, the MPC-based V2G operation in the MES is tested, with $v_j^{\text{ref}} = 0.97$ p.u., $T_s = 5$ s, and $c^{e,\text{avg}} = 100$ € /MWh. Given the limited V2G connection time (PLUG_{v2g}) and the similar function of BAT unit, the MPC simultaneously controls both the BAT and V2G EVs. To maximize the overall benefits of both units, the BAT is assigned a lower control priority once V2G EVs are connected.

Figs. 9 and 10 depict the 24-h thermal and electrical profiles of the MES, separately. In Fig. 9, with the same operational costs, the thermal generation of B, HP, and CHP match those in Case 1, except for 13:00–15:00. During this period, HPs are able to run at maximum output thanks to the improved voltage profiles (see Fig. 10) resulting from V2G operation.

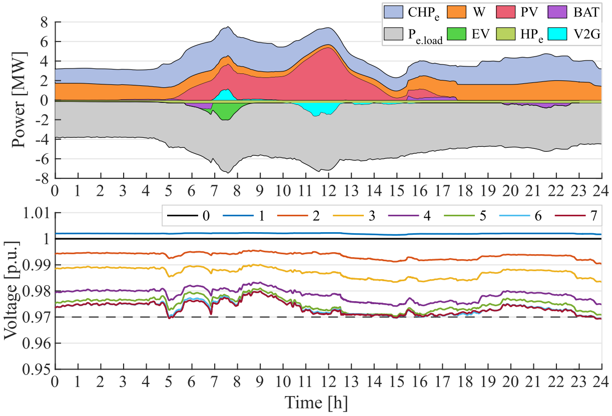

FIGURE 10. **Case 3: 24-h electrical demand and supply profiles (top) and voltage curves (bottom).**

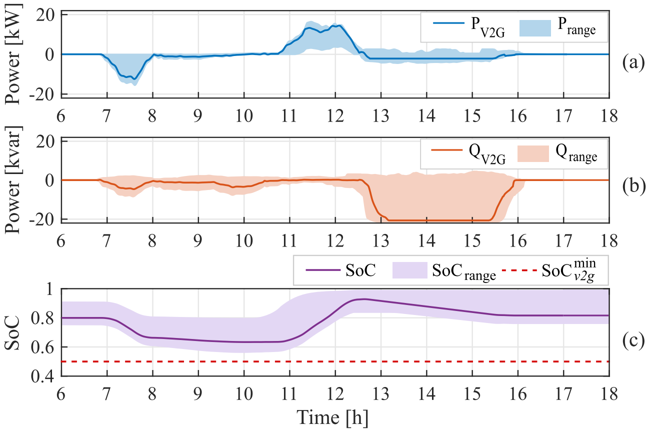

FIGURE 11. **(a) and (b) V2G charger profiles. (c) V2G EV SoC dynamics.**

In Fig. 10, compared to Cases 1 and 2, similar electric load and supply are performed, except the V2G operation (cyan). As can be seen, the voltage of all nodes remains within the reference range throughout the day. From 7:00 to 8:00, the voltage drop caused by increased EV charging demand (green) is alleviated by discharging the V2G EVs (cyan). Around 12:00, when MES output is high, the V2G chargers switch to charging mode to store the surplus power, thereby improving the utilization of MES units, like PV. After 13:00, even as MES generation declines, the network voltage remains within the reference range due to the reactive power support provided by the V2G chargers. In addition, when the V2G EVs are disconnected between 16:00 and 18:00, the operation of the BAT (purple) further stabilizes the voltage profile.

Fig. 11 shows the V2G charger profiles (a)–(b) and the V2G EV SoC dynamics (c). In (a) and (b), the blue and orange curves represent the active and reactive power of one V2G charger at node 5, respectively. The shaded area, $P_{\text{range}}/Q_{\text{range}}$, indicates the profile of all V2G chargers. During the peak load period (7:00–8:00), the V2G controller discharges EV batteries (blue) to compensate the increasing load demand. After 9:00, when the MES operates in a healthy state, the V2G system switches to "Power loss reduction" mode, using reactive power from V2G chargers (orange) to minimize power losses. Around 12:00, when the MES experiences surplus generation, V2G chargers absorb active power by charging the EV batteries. In addition, when voltage drops occur between 13:00 and 17:00, the "voltage control" mode is activated, using reactive power to stabilize the voltage. Meanwhile, the use of active power is limited by the V2G contract ($\text{DIS}_{\text{v2g}} = 1$, and $\text{PLUG}_{\text{v2g}} = 6$ h), which prevents unacceptable battery degradation. As a result, the leaving SoC of all EVs (shaded purple) remains above the minimum value $\text{SoC}^{\text{min}}_{\text{v2g}} = 0.5$, depicted with red dashed line in (c). Moreover, the initial SoC and final SoC of all EVs in three cases are presented in Table 3.

TABLE 3. **Initial and Final SoC of All EVs in Three Cases**

	Initial SoC [%]	Final SoC [%]
Case 1: No V2G	75∼90	100
Case 2: Smart Charging	75∼90	100
Case 3: V2G	75∼90	79∼100

TABLE 4. **Performance of MES in Three Cases**

Case	Voltage violation	Electrical [MWh]				Thermal [MWh]		
		E_{Loss}	E_{grid}	$E_{\text{PV/W}}$	E_{CHP}	E_{CHP}	E_{HP}	E_{B}
1	8 [hour]	3.18	19.5	54.6	51.4	52.2	19.5	20.6
2	5 [hour]	2.79	18.3	54.6	51.4	52.2	19.5	20.6
3	0.3 [hour]	2.52	17.2	54.6	50.4	51.1	21.7	19.5

Table 4 presents a comparison of the MES performance in three cases. As can be seen, voltage violation duration falls notably from 8 h in Case 1 to 0.3 h in Case 3, indicating effective voltage regulation by V2G. Correspondingly, power losses E_{Loss} decrease from 3.18 MWh in Case 1 to 2.52 MWh in Case 3, and grid imports E_{grid} drop from 19.5 to 17.2 MWh, while renewable generation $E_{\text{PV/W}}$ remains stable at 54.6 MWh. On the thermal side, HP output E_{HP} increases from 19.5 MWh in Case 1 to 21.7 MWh in Case 3, as thermal production from CHP and Boiler correspondingly declines. Overall, Case 3 with V2G achieves the best performance by minimizing voltage violations, losses, and grid dependence while shifting thermal supply toward more efficient HP operation.

D. LARGE SYSTEM TESTING AND ANALYSIS

As shown in Fig. 12, the IEEE 123-node test feeder [36] has been modified to represent a large MES comprising 242 classic EV chargers and 248 V2G chargers. Since this system is used to test the scalability of the proposed V2G control strategy for large-scale applications, the locations of energy components and EV chargers are assigned randomly. Considering the cable and power constraints of the IEEE 123-node system, the power profiles of the MES components are kept identical to those in Table 1 and Fig. 6 and 7, with the total number of EVs set to 500. All unbalanced loads are balanced by approximating the load in each of the three phases with the

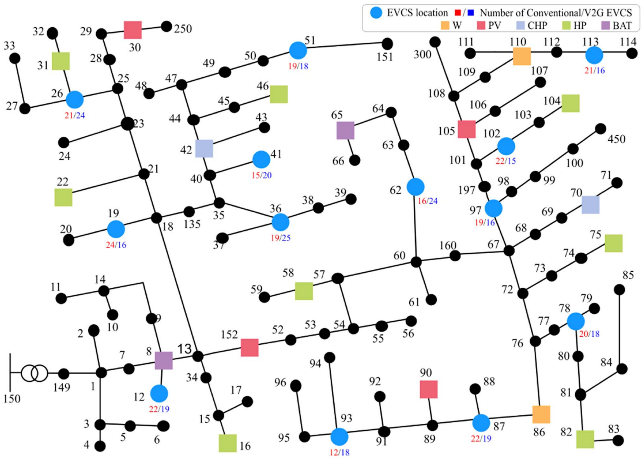

FIGURE 12. MES based on the modified IEEE 123-node test feeder.

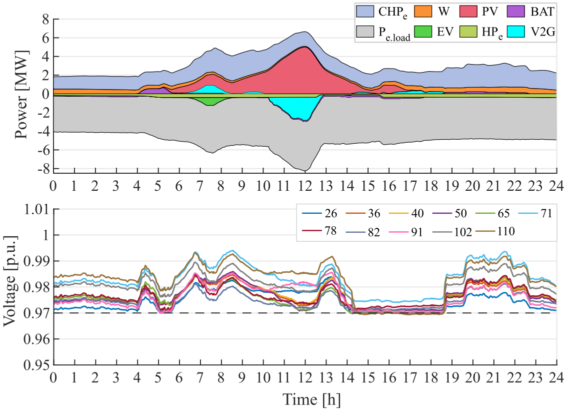

FIGURE 13. 24-h electrical power (top) and voltage profiles (bottom) for the IEEE 123-node MES.

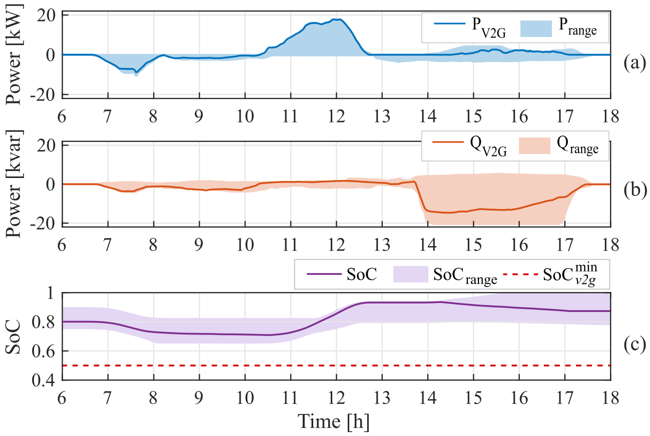

FIGURE 14. (a) and (b) V2G charger profiles. (c) V2G EV SoC dynamics.

TABLE 5. Comparison Between seven-Node and the 123-Node MES

System size	MPC setup	T_s	Computing time	N_{dec}	T_{comm}
7-node	k_c/k_p=10/30	5 [s]	2.53∼3.45 [s]	2790	1-2 [ms]
123-node	k_c/k_p=10/30	30 [s]	7.25∼10.68 [s]	7440	5-10 [ms]

maximum load, and the load profiles are obtained by scaling the data from Case 1 in Fig. 7. The V2G contract and EV profiles are the same as in Case 3. Moreover, the values of v_j^{ref}, k_c, k_p, and T_s are set to 0.97 p.u., 10, 30, and 30 s, respectively. The active power profiles of the MES and the voltage curves of 11 representative nodes are shown in Fig. 13. The proposed controller enables the V2G chargers (cyan) to effectively mitigate voltage violations during the peak charging period from 7:00 to 9:00 and periods of low PV/Wind generation between 13:00 and 16:00. Moreover, around 12:00, the surplus power generated by PVs (red) can be stored in EV batteries via V2G chargers.

Fig. 14 shows the active and reactive power of all V2G chargers, as well as the SoC dynamics of all EVs. Due to the similar MES generation and load profiles, the active power (blue) and reactive power (orange) of V2G chargers exhibit a trend similar to that observed in Case 3. The V2G chargers operate cost efficiently during their connection time, and active power regulation (blue) is limited by the V2G contract (DIS$_{\mathrm{v2g}} = 1$, and PLUG$_{\mathrm{v2g}} = 6$ h.). Meanwhile, the reactive power regulation (orange) after 14:00 ensures that both voltage profiles and all V2G EVs maintain acceptable range (above $v_j^{\mathrm{ref}} = 0.97$ p.u., and $\mathrm{SoC}_{\mathrm{v2g}}^{\min} = 50\%$).

In this article, the computational complexity mainly depends on the number of V2G chargers Π and the control horizon k_c. For example, in Case 3, with $\Pi = 93$ and $k_c = 10$, the QP problem involves $3 \times \Pi \times k_c = 2790$ decision variables, indicating $P_{j,v2g}^{\mathrm{ref.ch}}$, $P_{j,v2g}^{\mathrm{ref.dch}}$, and $Q_{j,v2g}^{\mathrm{ref}}$ over the prediction horizon. As a result, the computing time to solve the optimization problem at each control interval (T_s) ranges from 2.53 to 3.45 s.

However, in the IEEE 123-node MES, with $\Pi = 248$ V2G EVs, the decision variable increases from 2790 to 7440, which significantly raises the computational burden during real-time operation, resulting in computing times of 7.25 to 10.68 s. To address this issue, a longer control interval of $T_s = 30$ s can be used. Moreover, the computation of the optimization can be distributed across multiple processing units, as discussed for instance in [37].

On the other hand, communication issues also remain practical. In the IEEE 123-node MES with 500 EVs, each EV charger transmits four signals, including SoC, $P_{\mathrm{v2g}}^{\mathrm{ch/dch}}$, and Q_{v2g}. Considering that each signal stored in a “float” data type occupies 4 bytes, the total data volume per cycle is $4 \times 4 \times 500 = 8000$ bytes ≈ 8 kB. Given a communication device with a speed of 50–200 Mbps and considering communication delays, the data can be transmitted within 0.1–2 s, making it feasible for control intervals of $T_s = 30$ s. However, the servers where the data are aggregated can experience congestion and overload, which could be solved by implementing advanced load-balancing strategies to manage distributed message brokers [38].

Table 5 presents the control performance for both the FZJ seven-node MES and the IEEE 123-node MES. The computing time refers to the time required to solve the optimization problem at each control interval (T_s). The table shows that the computing time increases from 2.53–3.45 s for the seven-node MES to 7.25–10.68 s for the 123-node MES, indicating that computational complexity grows with the number of decision variables (N_{dec}). Meanwhile, based on the data transfer speed (50–200 Mbps), the communication time (T_{comm}) is estimated to increase from 1–2 ms to 5–10 ms. In the 123-node MES, the control interval is initially defined as $T_s = 30$ s to ensure sufficient computing time. The results show that $T_s = 30$ s is adequate for the increased number of decision variables, with computing times ranging from 7.25 to 10.68 s. Therefore, the proposed MPC maintains computational efficiency and reliable real-time performance, confirming its effective scalability for larger systems.

VI. CONCLUSION

This article presents an MPC-based multifunctional V2G operation in the MES. A novel formulation is designed that integrates four-quadrant V2G chargers, EV interactions, and MES limits, thereby enabling functions such as voltage regulation, power loss reduction, and MES cooperation. Moreover, this approach enhances the efficient use of MES components, such as PVs and HPs.

The MPC combined with the V2G mode regulator ensures efficient and real-time V2G operation in the MES. Three test cases based on the FZJ MES confirmed that the proposed V2G strategy enhances energy utilization, voltage profile, and overall MES performance. The extended test in the IEEE 123-node MES verifies the scalability of the proposed V2G framework in large systems.

Future studies will focus on coordinating the control of the electric and thermal components, including V2G EVs and HPs, in the large-scale MES.

REFERENCES

[1] X. Tian, C. An, and Z. Chen, “The role of clean energy in achieving decarbonization of electricity generation, transportation, and heating sectors by 2050: A meta-analysis review,” *Renew. Sustain. Energy Rev.*, vol. 182, 2023, Art. no. 113404.

[2] R. P. Upputuri and B. Subudhi, “A comprehensive review and performance evaluation of bidirectional charger topologies for V2G/G2V operations in EV applications,” *IEEE Trans. Transp. Electrific.*, vol. 10, no. 1, pp. 583–595, Jan. 2024.

[3] J. Jaworski, N. Zheng, M. Preindl, and B. Xu, “Vehicle-to-grid fleet service provision considering nonlinear battery behaviors,” *IEEE Trans. Transp. Electrific.*, vol. 10, no. 2, pp. 2945–2955, Feb. 2024.

[4] H. Liang, Y. Liu, F. Li, and Y. Shen, “Dynamic economic/emission dispatch including PEVs for peak shaving and valley filling,” *IEEE Trans. Ind. Electron.*, vol. 66, no. 4, pp. 2880–2890, Apr. 2018.

[5] Y. Sun, H. Yue, J. Zhang, and C. Booth, “Minimization of residential energy cost considering energy storage system and EV with driving usage probabilities,” *IEEE Trans. Sustain. Energy*, vol. 10, no. 4, pp. 1752–1763, Apr. 2018.

[6] L. Jorge, H. Concepcion, M. A. Arjona, M. Lesedi, and C. Ambrish, “Performance evaluation of an active neutral-point-clamped multilevel converter for active filtering in G2V-V2G and V2H applications,” *IEEE Access*, vol. 10, pp. 41607–41621, 2022.

[7] E. Akhavan-Rezai, M. F. Shaaban, E. F. El-Saadany, and F. Karray, “Managing demand for plug-in electric vehicles in unbalanced LV systems with photovoltaics,” *IEEE Trans. Ind. Informat.*, vol. 13, no. 3, pp. 1057–1067, Mar. 2017.

[8] C. Tan, Q. Chen, L. Zhang, and K. Zhou, “Frequency-adaptive repetitive control for three-phase four-leg V2G inverters,” *IEEE Trans. Transp. Electrific.*, vol. 7, no. 4, pp. 2095–2103, Apr. 2021.

[9] M. C. Kisacikoglu, B. Ozpineci, and L. M. Tolbert, “EV/PHEV bidirectional charger assessment for V2G reactive power operation,” *IEEE Trans. Power Electron.*, vol. 28, no. 12, pp. 5717–5727, Dec. 2013.

[10] Y. Wang, D. Qiu, G. Strbac, and Z. Gao, “Coordinated electric vehicle active and reactive power control for active distribution networks,” *IEEE Trans. Ind. Informat.*, vol. 19, no. 2, pp. 1611–1622, Feb. 2023.

[11] Q. Hu, S. Bu, and V. Terzija, “A distributed P and Q provision-based voltage regulation scheme by incentivized EV fleet charging for resistive distribution networks,” *IEEE Trans. Transp. Electrific.*, vol. 7, no. 4, pp. 2376–2389, Apr. 2021.

[12] D. Liu, E. De Din, D. Carta, and A. Benigni, “Controller hardware-in-the-loop testing of a multitimescale control architecture for multienergy systems,” *IEEE J. Emerg. Sel. Top. Ind. Electron.*, vol. 6, no. 2, pp. 499–510, Feb. 2025.

[13] H. Fan, D. Wang, Z. Yu, and L. Du, “Bilevel optimal scheduling of electric bus fleets in regional integrated electricity–gas–heat energy systems,” *IEEE Trans. Transp. Electrific.*, vol. 9, no. 2, pp. 2792–2807, Feb. 2023.

[14] D. Liu, D. Carta, A. Xhonneux, D. Müller, and A. Benigni, “Short-term control of heat pumps to support power grid operation,” *IEEE Open J. Ind. Electron. Soc.*, vol. 5, pp. 1221–1238, 2024.

[15] C. Li, D. Carta, and A. Benigni, “EV charging station placement considering V2G and human factors in multi-energy systems,” *IEEE Trans. Smart Grid*, vol. 16, no. 1, pp. 529–540, Jan. 2025.

[16] T. Morstyn, B. Hredzak, R. P. Aguilera, and V. G. Agelidis, “Model predictive control for distributed microgrid battery energy storage systems,” *IEEE Trans. Control Syst. Technol.*, vol. 26, no. 3, pp. 1107–1114, Mar. 2017.

[17] C.-F. Lu, G.-P. Liu, Y. Yu, and J. Cui, “A coordinated model predictive control-based approach for vehicle-to-grid scheduling considering range anxiety and battery degradation,” *IEEE Trans. Transp. Electrific.*, vol. 11, no. 2, pp. 5688–5699, Apr. 2025.

[18] L. Guo, Z. Xu, N. Jin, Y. Chen, Y. Li, and Z. Dou, “An inductance online identification method for model predictive control of V2G inverter with enhanced robustness to grid frequency deviation,” *IEEE Trans. Transp. Electrific.*, vol. 8, no. 2, pp. 1575–1589, Feb. 2022.

[19] S. Ke et al., “A frequency control strategy for EV stations based on MPC-VSG in islanded micro-grids,” *IEEE Trans. Ind. Informat.*, vol. 20, no. 2, pp. 1819–1831, Feb. 2023.

[20] N. Mignoni, R. Carli, and M. Dotoli, “Distributed noncooperative MPC for energy scheduling of charging and trading electric vehicles in energy communities,” *IEEE Trans. Control Syst. Technol.*, vol. 31, no. 5, pp. 2159–2172, Sep. 2023.

[21] J. Hu, C. Ye, Y. Ding, J. Tang, and S. Liu, “A distributed MPC to exploit reactive power V2G for real-time voltage regulation in distribution networks,” *IEEE Trans. Smart Grid*, vol. 13, no. 1, pp. 576–588, Jan. 2021.

[22] E. A. M. Ceseña and P. Mancarella, “Energy systems integration in smart districts: Robust optimisation of multi-energy flows in integrated electricity, heat and gas networks,” *IEEE Trans. Smart Grid*, vol. 10, no. 1, pp. 1122–1131, Jan. 2018.

[23] M. Farivar and S. H. Low, “Branch Flow model: Relaxations and convexification—Part I,” *IEEE Trans. Power Syst.*, vol. 28, no. 3, pp. 2554–2564, Mar. 2013.

[24] M. Wenzel, E. De Din, M. Zimmer, and A. Benigni, “Gaussian process supported stochastic MPC for distribution grids,” *IEEE Open J. Control Syst.*, vol. 4, pp. 332–348, 2025.

[25] P. Yu, C. Wan, M. Sun, Y. Zhou, and Y. Song, “Distributed voltage control of active distribution networks with global sensitivity,” *IEEE Trans. Power Syst.*, vol. 37, no. 6, pp. 4214–4228, Jun. 2022.

[26] Z. Li, L. Wu, Y. Xu, S. Moazeni, and Z. Tang, “Multi-stage real-time operation of a multi-energy microgrid with electrical and thermal energy storage assets: A data-driven MPC-ADP approach,” *IEEE Trans. Smart Grid*, vol. 13, no. 1, pp. 213–226, Jan. 2021.

[27] I. del Hoyo Arce, S. H. López, S. L. Perez, M. Rämä, K. Klobut, and J. A. Febres, “Models for fast modelling of district heating and cooling networks,” *Renew. Sustain. Energy Rev.*, vol. 82, pp. 1863–1873, 2018.

[28] Y. Guo, H. Gao, Q. Wu, H. Zhao, J. Østergaard, and M. Shahidehpour, “Enhanced voltage control of VSC-HVDC-Connected offshore wind farms based on model predictive control,” *IEEE Trans. Sustain. Energy*, vol. 9, no. 1, pp. 474–487, Jan. 2017.

[29] A. Yazdani and R. Iravani, *Voltage-Sourced Converters in Power Systems: Modeling, Control, and Applications.* Hoboken, NJ, USA: Wiley, 2010.

[30] S. Wang, Q. Liu, and X. Ji, "A fast sensitivity method for determining line loss and node voltages in active distribution network," *IEEE Trans. Power Syst.*, vol. 33, no. 1, pp. 1148–1150, Jan. 2017.

[31] A. Verma, B. Singh, A. Chandra, and K. Al-Haddad, "An implementation of solar PV array based multifunctional EV charger," *IEEE Trans. Ind. Appl.*, vol. 56, no. 4, pp. 4166–4178, Jul./Aug. 2020.

[32] K. Schönleber, C. Collados, R. T. Pinto, S. Ratés-Palau, and O. Gomis-Bellmunt, "Optimization-based reactive power control in HVDC connected wind power plants," *Renew. Energy*, vol. 109, pp. 500–509, 2017.

[33] X. Zhou, M. Farivar, Z. Liu, L. Chen, and S. H. Low, "Reverse and forward engineering of local voltage control in distribution networks," *IEEE Trans. Autom. Control*, vol. 66, no. 3, pp. 1116–1128, Mar. 2021.

[34] L. Wang, *Model Predictive Control System Design and Implementation Using MATLAB.* London, U.K.: Springer, 2009.

[35] C. Li, D. Carta, and A. Benigni, "A real-time simulation framework to evaluate the scheduling of V2G in distribution networks," in *48th Annu. Conf. IEEE Ind. Electron. Soc.*, 2022, pp. 1–6.

[36] K. P. Schneider et al., "Analytic considerations and design basis for the IEEE distribution test feeders," *IEEE Trans. Power Syst*, vol. 33, no. 3, pp. 3181–3188, Mar. 2017.

[37] J. Rivera, C. Goebel, and H.-A. Jacobsen, "Distributed convex optimization for electric vehicle aggregators," *IEEE Trans. Smart Grid*, vol. 8, no. 4, pp. 1852–1863, Apr. 2017.

[38] A. Detti, L. Funari, and N. Blefari-Melazzi, "Sub-linear scalability of MQTT clusters in topic-based publish-subscribe applications," *IEEE Trans. Netw. Serv. Manage.*, vol. 17, no. 3, pp. 1954–1968, Mar. 2020.

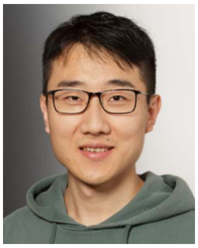

CHUAN LI (Student Member, IEEE) received the B.Sc. degree in electrical engineering from Hebei Agricultural University, Baoding, China, in 2014, and the M.Sc. degree in electrical engineering from the Chalmers University of Technology, Gothenburg, Sweden, in 2021. He is currently working toward the Ph.D. degree with the "Institute of Climate and Energy Systems, Energy Systems Engineering (ICE-1)," Forschungszentrum Jülich, Jülich, Germany.

DANIELE CARTA (Member, IEEE) received the B.Sc. and M.Sc. degrees in electrical engineering in 2013 and 2016, respectively, and the Ph.D. degree in electrical engineering in 2020, all from the University of Cagliari, Cagliari, Italy.

He is currently the Department Leader of the "Control Solution" Group, "Institute of Climate and Energy Systems, Energy Systems Engineering (ICE-1)," Forschungszentrum Jülich, Jülich, Germany.

EDOARDO DE DIN (Member, IEEE) received the B.Sc. and M.Sc. degrees in electrical engineering from the University of Trieste, Trieste, Italy, in 2013 and 2015, respectively, and the Ph.D. degree in electrical engineering from RWTH-Aachen University, Aachen, Germany, in 2023.

He is currently with the "Control Solution" Group, "Institute of Climate and Energy Systems: Energy Systems Engineering (ICE-1)," Forschungszentrum Jülich, Jülich, Germany.

ANDREA BENIGNI (Senior Member, IEEE) received the B.Sc. and M.Sc. degrees in electrical engineering from the Politecnico di Milano, Milano, Italy, in 2005 and 2008, respectively, and the Ph.D. degree in electrical engineering from RWTH-Aachen University, Aachen, Germany, in 2013.

From 2014 to 2019, he was an Assistant Professor with the Department of Electrical Engineering, University of South Carolina, Columbia, SC, USA. Since 2019, he has been a Full Professor with RWTH-Aachen University and Director of the "Institute of Climate and Energy Systems, Energy Systems Engineering (ICE-1)," Forschungszentrum Jülich, Jülich, Germany.